High-dimensional one-way quantum processing implemented on d-level cluster states

Christian Reimer[1,2,*], Stefania Sciara[1,3], Piotr Roztocki[1], Mehedi Islam[1], Luis Romero Cortés[1], Yanbing Zhang[1], Bennet Fischer[1], Sébastien Loranger[4], Raman Kashyap[4,5], Alfonso Cino[3], Sai T. Chu[6], Brent E. Little[7], David J. Moss[8], Lucia Caspani[9], William J. Munro[10], José Azaña[1], Michael Kues[1,11,*,+], and Roberto Morandotti[1,12,13,+]

[1]Institut National de la Recherche Scientifique (INRS-EMT), 1650 Blvd. Lionel-Boulet, Varennes, J3X1S2, Canada
[2]John A. Paulson School of Engineering and Applied Sciences, Harvard University, Cambridge, 02138, USA
[3]Department of Energy, Information Engineering and Mathematical Models, University of Palermo, Palermo, Italy
[4]Engineering Physics Department, Polytechnique Montreal, 2900 Blvd. Édouard-Montpetit, Montreal H3T 1J4, Canada
[5]Electrical Engineering Department, Polytechnique Montreal, 2900 Blvd. Édouard-Montpetit, Montreal H3T 1J4, Canada
[6]Department of Physics and Material Science, City University of Hong Kong, Tat Chee Avenue, Hong Kong, China
[7]State Key Laboratory of Transient Optics and Photonics, Xi'an Institute of Optics and Precision Mechanics, Chinese Academy of Science, Xi'an, China
[8]Centre for Micro Photonics, Swinburne University of Technology, Hawthorn, Victoria 3122, Australia
[9]Institute of Photonics, Department of Physics, University of Strathclyde, Glasgow G1 1RD, UK
[10]NTT Basic Research Laboratories, NTT Corporation, 3-1 Morinosato-Wakamiya, Kanagawa, 243-0198, Japan
[11]School of Engineering, University of Glasgow, Rankine Building, Oakfield Avenue, Glasgow G12 8LT, UK
[12]Institute of Fundamental and Frontier Sciences, University of Electronic Science and Technology of China, Chengdu 610054, China
[13]National Research University of Information Technologies, Mechanics and Optics, St Petersburg, Russia
*these authors contributed equally
[+]michael.kues@glasgow.ac.uk, [+]morandotti@emt.inrs.ca

Quantum mechanics can resolve important problems, such as executing certain computational tasks exponentially faster than classical computers[1] and to perform measurements with precision exceeding the classical limit[2,3]. Of significant interest are cluster states[4], which can enable the realization of universal quantum computers by means of a 'one-way' scheme[5], where processing is performed through measurements[6]. The use of d-level cluster states can increase the quantum resources while keeping the number of parties constant[7] and enable novel algorithms[8]. Here, we achieve their experimental realization, characterization, and test their noise sensitivity. We create three-level, four-partite cluster states formed by two photons in the time[9] and frequency[10] domain and confirm genuine multi-partite entanglement with higher noise robustness compared to conventional two-level cluster states[6,11–13]. We perform high-dimensional one-way quantum computation operations, where the cluster states are transformed into different orthogonal, maximally entangled d-level two-partite states by means of projection measurements. Our scalable approach is based on integrated photonic chips[9,10] and optical fiber communication components and achieves new and deterministic functionalities.

Cluster states are a particularly important type of multi-partite states (i.e. those formed by more than two parties, like multiple atoms, photons, etc.) characterized by two unique properties: maximal connectedness[4] (i.e. any two parties of the state can be projected into a maximally entangled state through measurements on the remaining parties), as well as by the highest persistency of entanglement[4] (i.e. cluster states require a maximal number of projection measurements to fully destroy entanglement in the system). These properties make cluster states equivalent to universal one-way (also called measurement-based) quantum computers[5], where different algorithms can be implemented by performing measurements on the individual parties of

the cluster states[5,6]. This approach greatly simplifies quantum processing, since measurement settings can be usually implemented more easily than the gate operations required in other approaches[1,14]. Furthermore, cluster states have structural properties that protect the quantum information, i.e. they enable topological quantum error correction[11] for minimizing computation errors. Due to the significant importance of cluster states, they have been studied in many different platforms. In particular, experimental realizations can be separated into two classes: discrete *two*-level[6,11–13] (i.e. qubit) and continuous-variable[15,16] cluster states. Continuous-variable systems are intrinsically high-dimensional, and they can be achieved using squeezed states[15,16]. However, the quantum resource of these states relies on the level of squeezing, which is very sensitive to noise[17]. Further, in the framework of today's squeezed state realisation with bulk optical parametric oscillators, the individual quantum modes cannot be independently addressed. In contrast, discrete quantum states are less sensitive to noise than squeezed states[17], and even more importantly, the individual modes of the quantum states can be fully accessed and individually manipulated, making their use especially appealing.

Nevertheless, increasing the number of particles to boost the computational resource comes at the price of significantly reduced coherence times, detection rates, and increased sensitivity to noise. These limitations have restricted the realization of discrete cluster states to a record of eight qubits[11]. In a novel approach, the use of discrete but d-level entangled states has the potential to address several limitations of qubit cluster states. First, the quantum resource can be increased without changing the number of parties[7]; second, d-level quantum states enable the implementation of highly efficient computation protocols[8]; and third, which we show here, higher dimensions reduce the noise sensitivity of cluster states. The experimental realization of d-level multi-partite cluster states is the key missing piece required to exploit these important benefits for high-dimensional quantum computation[7]. Unfortunately, today's established quantum systems are ill-

suited for increasing the dimensionality of discrete multi-partite entangled states. For example, atomic[18] and superconducting[19] systems are mainly based on qubit schemes, and demonstrated high-dimensional photonic systems[20,21] become experimentally complex, inefficient and typically suffer from degraded state purity when the number of photons used increases. The only d-level quantum states with more than two parties generated so far are three-level, three-photon states in a bulk, free-space setup[22]. Cluster states with two and three parties are equivalent to *Bell* and *GHZ* states, respectively[4], while genuine discrete d-level cluster states require at least four parties[4]. To date, these states have not been realized, nor have their entanglement properties and their tolerance to noise been investigated.

Here, we present a general approach to prepare and coherently manipulate discrete d-level multi-partite quantum systems based on the simultaneous entanglement – i.e. hyper-entanglement[23] – of two photons in time and frequency, by exploiting integrated photonic chips combined with fiber-optics telecommunications components[9,10]. Using this method, we present the first experimental realization and characterization of qudit cluster states. Further, we use these states to perform high-dimensional one-way quantum processing.

As a basis for the generation of d-level clusters, we used intrinsically linked and non-commuting observables, specifically photon frequency and time, to create hyper-entangled states that support higher dimensions. In contrast, hyper-entangled photon states have so far only been realized using combinations of independent degrees of freedom, described by commuting operators, such as polarization, optical paths and temporal modes[23–25]. In detail, we consider two discrete forms of energy-time entanglement, namely time-bin[9] and frequency-bin[10]. Time-bin entanglement refers to states where the photons are in a superposition of well-defined and distinct temporal modes, while frequency-bin entangled states are characterized by discrete and non-overlapping frequency modes. Time-bin entanglement can be generated by exciting a spontaneous

parametric process in an optical nonlinear medium with multiple phase-locked pulses[9], see Fig. 1a). On the other hand, frequency-bin entanglement can be realized when the nonlinear medium is placed within an optical resonator, where the emission bandwidth covers multiple resonances[10], see Fig. 1b). Remarkably, if the time scales (and frequency separations) corresponding to the individual modes are different, frequency-bin and time-bin entanglement become independent, allowing one to generate hyper-entangled, multi-partite states. Such hyper-entangled states can be produced by exciting the nonlinear element, placed inside the resonator, with a coherent set of multiple pulses, see Fig. 1c), as long as the pulse separation is much larger than the photon lifetime in the resonator. In this case, the time-bin component can be fully controlled in the temporal domain, while the frequency-bin component can be completely and independently controlled in the frequency domain.

In our experimental implementation, we produced photon pairs using the nonlinear process of spontaneous four-wave mixing within a microring resonator, see Methods. By exciting the resonator with three phase-locked pulses and considering three frequency mode pairs, we generated photon states simultaneously entangled in time and frequency, described by the following expression (Eq. 1):

$$\begin{aligned}\left|\Psi_{\mathrm{Hyper}}\right\rangle &= (|1_s,1_i\rangle + |2_s,2_i\rangle + |3_s,3_i\rangle) \otimes (|\mathrm{a}_s,\mathrm{a}_i\rangle + |\mathrm{b}_s,\mathrm{b}_i\rangle + |\mathrm{c}_s,\mathrm{c}_i\rangle) \\ &= |1_s,1_i,\mathrm{a}_s,\mathrm{a}_i\rangle + |1_s,1_i,\mathrm{b}_s,\mathrm{b}_i\rangle + |1_s,1_i,\mathrm{c}_s,\mathrm{c}_i\rangle \\ &\quad + |2_s,2_i,\mathrm{a}_s,\mathrm{a}_i\rangle + |2_s,2_i,\mathrm{b}_s,\mathrm{b}_i\rangle + |2_s,2_i,\mathrm{c}_s,\mathrm{c}_i\rangle \\ &\quad + |3_s,3_i,\mathrm{a}_s,\mathrm{a}_i\rangle + |3_s,3_i,\mathrm{b}_s,\mathrm{b}_i\rangle + |3_s,3_i,\mathrm{c}_s,\mathrm{c}_i\rangle,\end{aligned}$$

where numbers indicate time-bins and letters indicate frequency-bins with the indices *s* and *i* referring to the signal and idler photons, respectively (the normalization is not shown for compactness). This hyper-entangled state is bi-separable, since any projection measurement performed in, e.g., the time-bin basis, does not affect the frequency-bin entangled sub-state (and

vice versa). In contrast, a cluster state is characterized by the fact that a projection measurement of one party affects the remaining portion of the state. An ideal compact three-level cluster state can be obtained by judiciously modifying the phase terms in Eq. 1, which then reads (Eq. 2):

$$\begin{aligned}|\Psi_{\text{Cluster}}\rangle \;=\; & |1_s,1_i,\mathrm{a}_s,\mathrm{a}_i\rangle + |1_s,1_i,\mathrm{b}_s,\mathrm{b}_i\rangle + |1_s,1_i,\mathrm{c}_s,\mathrm{c}_i\rangle \\ & + |2_s,2_i,\mathrm{a}_s,\mathrm{a}_i\rangle + e^{i\frac{2\pi}{3}}|2_s,2_i,\mathrm{b}_s,\mathrm{b}_i\rangle + e^{-i\frac{2\pi}{3}}|2_s,2_i,\mathrm{c}_s,\mathrm{c}_i\rangle \\ & + |3_s,3_i,\mathrm{a}_s,\mathrm{a}_i\rangle + e^{-i\frac{2\pi}{3}}|3_s,3_i,\mathrm{b}_s,\mathrm{b}_i\rangle + e^{i\frac{2\pi}{3}}|3_s,3_i,\mathrm{c}_s,\mathrm{c}_i\rangle.\end{aligned}$$

In order to experimentally transform the hyper-entangled state (Eq. 1) into this cluster state (Eq. 2), access to the individual terms of the state is necessary, while maintaining coherence. For multi-particle states this is technically very challenging, requiring two-party quantum gates, which are usually probabilistic[26]. The hyper-entangled time-frequency approach allows for a deterministic and coherent implementation of this operation. Specifically, since we are employing two different types of discrete energy-time entanglement associated with different time scales (i.e. time-bin and frequency-bin), it is possible to fully map the entangled state into the time-domain to perform state manipulations using synchronized electro-optic modulation. The realized gate (see Fig. 2) provides coherent access to the individual state terms. The frequency-to-time mapping was performed by a fiber Bragg grating array placed in a self-referenced and phase-stable loop configuration, see Methods. By choosing the appropriate phase pattern (see Fig. 2), the bi-separable hyper-entangled state was transformed into a three-level four-partite cluster state.

To confirm genuine multi-partite entanglement, we determined an optimal entanglement witness $\mathcal{W}_{opt}^{(\mathcal{C}_{4,3})} = \frac{1}{2}\mathbb{I} - \frac{3}{2}|C\rangle\langle C|$, where $\mathbb{I}$ is the identity operator and $|C\rangle$ the wavefunction of the cluster state, see Methods. This witness detects the presence of a cluster state when its expectation value is negative (a minimum of -1 is reached by a theoretically optimal cluster state, i.e. in the absence of imperfection or noise contributions). This witness can be reduced to a measurable

witness $\mathcal{W}_{2S}^{(\mathcal{C}_{4,3})}$, containing two orthogonal measurement settings represented by the generalized three-dimensional Pauli matrices *X* and *Z*, see Methods. To experimentally determine the expectation value of the cluster state witness, given by (Eq. 3)

$$\langle \mathcal{W}_{2S}^{(\mathcal{C}_{4,3})} \rangle = \frac{5}{3} - \frac{1}{3} Re\big(\langle \mathbb{I}_1 \mathbb{I}_2 Z_3 Z_4^\dagger \rangle + \langle Z_1^\dagger Z_2 \mathbb{I}_3 \mathbb{I}_4 \rangle + \langle \mathbb{I}_1 Z_2 X_3 X_4 \rangle + \langle \mathrm{X}_1 X_2 Z_3 \mathbb{I}_4 \rangle + \langle Z_1 \mathbb{I}_2 X_3 X_4 \rangle + \langle Z_1^\dagger Z_2^\dagger X_3 X_4 \rangle + \langle X_1 X_2 \mathbb{I}_3 Z_4 \rangle + \langle X_1 X_2 Z_3^\dagger Z_4^\dagger \rangle\big),$$

we measured the diagonal elements of the density matrix (see Fig. 3a), as well as the expectation values of the eight witness terms individually (see Fig. 3b). This was achieved by means of projection measurements implemented by imbalanced interferometers and electro-optical modulators, see Methods. We measured a witness expectation value of $\langle \mathcal{W}_{2S}^{(\mathcal{C}_{4,3})} \rangle = -0.28 \pm 0.04$, confirming (within the range of 7 standard deviations) the presence of a cluster state featured by genuine three-level multi-partite entanglement.

We then tested the impact of incoherent, phase and amplitude noise on the state with respect to the expectation value of the witness. Monte Carlo simulations, based on the experimental values, were performed to estimate the distribution of the expectation values of the witness operator with respect to different noise sources (see Fig. 3 c-e). We also simulated the threshold for which the states lose their cluster-state properties due to the impact of noise. We found that our d-level cluster states are highly robust and can tolerate up to 66.6% of incoherent noise with respect to the optimal witness and 37.5% for the measured witness. In addition, they can also endure high amounts of amplitude and phase noise, i.e. as much as 83% (55% for the measured witness) average amplitude fluctuations, and up to 37% (25%) error in the phase terms (see Fig. 3 c-e). Most remarkably, our finding show that d-level cluster states are significantly more robust towards noise compared to two-level states. In comparison, a four-qubit cluster state can only tolerate 50% incoherent noise with respect to the optimal witness and 33% for the measurement witness, while a six-qubit cluster

state (having slightly lower computational power compared to the here demonstrated four-qutrit state) can only tolerate 50% for the optimal and 28.5% for the measurement witness, see Methods. Our findings therefore show that d-level cluster states not only increase the quantum resource, but also provide better noise tolerance compared to qubit cluster states with comparable computational power.

To confirm the potential of d-level cluster states for quantum computation, we demonstrated that different and orthogonal entangled states can be generated by simply performing projection measurements on the parties of the cluster, which is the working principle of one-way quantum computation[5,7]. Indeed, one-way quantum computation is implemented by projecting the remaining entangled state through subsequent measurements on the parties. We here show this shaping of the cluster states and transform them into different orthogonal bi-partite states. For this, we carried out two-partite projections in either the frequency or time domain, and verified, via quantum interference measurements, that the resultant states are mutually orthogonal and entangled. In detail, we projected on the frequency-bins $|\mathrm{a},\mathrm{a}\rangle$, $|\mathrm{b},\mathrm{b}\rangle$, or $|\mathrm{c},\mathrm{c}\rangle$ individually, and confirmed the generation of three-level time-bin entangled states $|\psi_{a,a}\rangle = |1,1\rangle + |2,2\rangle + |3,3\rangle$, $|\psi_{b,b}\rangle = |1,1\rangle + e^{i\frac{2\pi}{3}}|2,2\rangle + e^{-i\frac{2\pi}{3}}|3,3\rangle$, and $|\psi_{c,c}\rangle = |1,1\rangle + e^{-i\frac{2\pi}{3}}|2,2\rangle + e^{i\frac{2\pi}{3}}|3,3\rangle$, which are mutually orthogonal (see Fig. 4 a-c). Similarly, we projected on the time-bins $|1,1\rangle$, $|2,2\rangle$, or $|3,3\rangle$, and confirmed the generation of the orthogonal three-level frequency-bin entangled states $|\psi_{1,1}\rangle = |\mathrm{a},\mathrm{a}\rangle + |\mathrm{b},\mathrm{b}\rangle + |\mathrm{c},\mathrm{c}\rangle$, $|\psi_{2,2}\rangle = |\mathrm{a},\mathrm{a}\rangle + e^{i\frac{2\pi}{3}}|\mathrm{b},\mathrm{b}\rangle + e^{-i\frac{2\pi}{3}}|\mathrm{c},\mathrm{c}\rangle$, and $|\psi_{3,3}\rangle = |\mathrm{a},\mathrm{a}\rangle + e^{-i\frac{2\pi}{3}}|\mathrm{b},\mathrm{b}\rangle + e^{i\frac{2\pi}{3}}|\mathrm{c},\mathrm{c}\rangle$ (see Fig. 4 d-e). The orthogonality of these target states was confirmed by the relative phase shift in the respective quantum interference patterns. Furthermore, all measured raw visibilities - listed in the Extended Data Table 1 - violated their respective two-partite Bell inequalities, see Methods. Therefore, these projection measurements performed on a cluster state

represent high-dimensional one-way quantum computing operations. Future universal quantum computation will require the application of d-level Hadamard gates, that have already been achieved for time-bin qubits[27], as well as frequency-bin qubits and qutrits[28].

In conclusion, our results show that high-dimensional one-way quantum computation with discrete multi-partite entangled states is experimentally viable. The cluster state realization was enabled by the use of on-chip and fiber-telecommunication components that provide highly stable, scalable and, most importantly, deterministic operations. Furthermore, our work also shows that integration is not, as it is often regarded, simply limited to miniaturizing devices and reducing cost (typically at the expense of lower performance), but can in fact enable novel and powerful capabilities. Most significantly, our approach is advantageous compared to current methods based on two-level cluster states, since it can provide a better noise tolerance and a significant improvement in terms of an effective quantum resource rate (*EQRR*). In particular, multi-photon states that are generated by multiple spontaneous parametric processes are hampered by a decrease in state purity with increased photon number[29]. In contrast, our approach allows imprinting a multi-partite high-dimensional quantum system in a two-photon state with high purity, since only a single, efficient spontaneous parametric process is used. This allows increasing the amount of quantum information for each successfully detected two-photon event, which in turn can pave the way towards highly efficient and practical quantum computing systems. Here, the ability to implement active feed-forward to speed up the computation[30] when multiple parties are detected simultaneously will have to be addressed by means of targeted algorithms. In general, quantum systems suffer significant reduction in their coherence time or detection rate when the number of entangled particles is increased. As an example, the largest realized two-level cluster states to date were comprised of six[13] and eight[11] qubits. These states had Hilbert space sizes ($H_{N,D} = D^N$) of $H_{6,2}$ = 64 and $H_{8,2}$ = 256, and were featured by moderate (yet impressive for current technology) six-

and eight-photon detection rates (DR) of $DR_{6,2}$ = 12 mHz and $DR_{8,2}$ = 0.89 mHz, resulting in effective quantum resource rates ($EQRR_H = H * DR$) of $EQRR_{64}$ = 0.768 Hz and $EQRR_{256}$ = 0.228 Hz, respectively. In the multi-photon cluster state approach, the detection rate diminishes more than the gain obtained through the increase in Hilbert space size, thus reducing the *EQRR*. In contrast, we achieved a Hilbert space size of $H_{4,3}$ = 81 (corresponding to 6.34 qubits), yet at a much higher detection rate of $DR_{4,3}$ = 1 Hz, resulting in an $EQRR_{81}$ = 81 Hz. This corresponds to a hundred-fold increase with respect to the six-photon state. The Hilbert space size can be further enlarged by increasing the number of frequency and temporal modes, without compromising the detection rate. In turn, this further boosts the *EQRR*. For example, a moderate improvement to $D = 4$ will already lead to quantum states equivalent to 8 qubits ($H_{4,4}$ = 256) and enhancing the dimensionality to $D = 6$ will correspond to an equivalent of 10.3 qubits ($H_{4,6}$ = 1296), thus exceeding the largest multi-photon state (GHZ, with $EQRR_{1024}$ = 3.17 Hz) measured to date[29]. Finally, our approach exploits twice the same type of entanglement (i.e. energy-time) to increase the number of parties through hyper-entanglement. It should be possible to extend this concept to three (or even more) different and independent realizations of energy-time entanglement. This will allow boosting the number of parties, while still maintaining a two-photon state and the use of the same working principle based on deterministic quantum gates. Our work therefore provides an important step towards achieving powerful and noise tolerant quantum computation in a scalable and mass-producible platform.

References:

1. Lloyd, S. Universal quantum simulators. *Science* **273,** 1073–1078 (1996).
2. Israel, Y., Rosen, S. & Silberberg, Y. Supersensitive polarization microscopy using NOON states of light. *Phys. Rev. Lett.* **112,** 12–15 (2014).
3. Hodaei, H. *et al.* Enhanced sensitivity at higher-order exceptional points. *Nature* **548,** 187 (2017).
4. Briegel, H. J. & Raussendorf, R. Persistent entanglement in arrays of interacting particles. *Phys. Rev. Lett.* **86,** 910–913 (2001).
5. Raussendorf, R. & Briegel, H. J. A one-way quantum computer. *Phys. Rev. Lett.* **86,** 5188–5191 (2001).
6. Walther, P. *et al.* Experimental one-way quantum computing. *Nature* **434,** 169–176 (2005).
7. Zhou, D., Zeng, B., Xu, Z. & Sun, C. Quantum computation based on d-level cluster state. *Phys. Rev. A* **68,** 062303 (2003).
8. Wang, D.-S., Stephen, D. T. & Raussendorf, R. Qudit quantum computation on matrix product states with global symmetry. *Phys. Rev. A* **95,** 032312 (2017).
9. Reimer, C. *et al.* Generation of multiphoton entangled quantum states by means of integrated frequency combs. *Science* **351,** 1176–1180 (2016).
10. Kues, M. *et al.* On-chip generation of high-dimensional entangled quantum states and their coherent control. *Nature* **546,** 622–626 (2017).
11. Yao, X.-C. *et al.* Experimental demonstration of topological error correction. *Nature* **482,** 489–94 (2012).
12. Lanyon, B. P. *et al.* Measurement-based quantum computation with trapped ions. *Phys. Rev. Lett.* **111,** 210501 (2013).
13. Lu, C. Y. *et al.* Experimental entanglement of six photons in graph states. *Nat. Phys.* **3,** 91–95 (2007).
14. Knill, E., Laflamme, R. & Milburn, G. J. A scheme for efficient quantum computation with linear optics. *Nature* **409,** 46–52 (2001).
15. Pysher, M., Miwa, Y., Shahrokhshahi, R., Bloomer, R. & Pfister, O. Parallel generation of quadripartite cluster entanglement in the optical frequency comb. *Phys. Rev. Lett.* **107,** 030505 (2011).

16. Yokoyama, S. *et al.* Ultra-large-scale continuous-variable cluster states multiplexed in the time domain. *Nat. Photonics* **7,** 982–986 (2013).
17. Lloyd, S. & Braunstein, S. L. Quantum computation over continuous variables. *Phys. Rev. Lett.* **82,** 1784–1787 (1999).
18. Blatt, R. & Wineland, D. Entangled states of trapped atomic ions. *Nature* **453,** 1008–1015 (2008).
19. Kandala, A. *et al.* Hardware-efficient variational quantum eigensolver for small molecules and quantum magnets. *Nature* **549,** 242–246 (2017).
20. Dada, A. C., Leach, J., Buller, G. S., Padgett, M. J. & Andersson, E. Experimental high-dimensional two-photon entanglement and violations of generalized Bell inequalities. *Nat. Phys.* **7,** 677–680 (2011).
21. Gräfe, M. *et al.* On-chip generation of high-order single-photon W-states. *Nat. Photonics* **8,** 791–795 (2014).
22. Malik, M. *et al.* Multi-photon entanglement in high dimensions. *Nat. Photonics* **10,** 248–252 (2016).
23. Barreiro, J., Langford, N., Peters, N. & Kwiat, P. Generation of hyperentangled photon pairs. *Phys. Rev. Lett.* **95,** 260501 (2005).
24. Chen, K. *et al.* Experimental realization of one-way quantum computing with two-photon four-qubit cluster states. *Phys. Rev. Lett.* **99,** 120503 (2007).
25. Vallone, G., Pomarico, E., Mataloni, P., Martini, F. De & Berardi, V. Realization and Characterization of a Two-Photon Four-Qubit Linear Cluster State. *Phys. Rev. Lett.* **98,** 180502 (2007).
26. O'Brien, J. L., Pryde, G. J., White, A. G., Ralph, T. C. & Branning, D. Demonstration of an all-optical quantum controlled-NOT gate. *Nature* **426,** 264–267 (2003).
27. Humphreys, P. C. *et al.* Linear optical quantum computing in a single spatial mode. *Phys. Rev. Lett.* **111,** 150501 (2013).
28. Lu, H.-H. *et al.* Electro-optic frequency beam splitters and tritters for high-fidelity photonic quantum information processing. *Phys. Rev. Lett.* **120,** 030502 (2018).
29. Wang, X. L. *et al.* Experimental ten-photon entanglement. *Phys. Rev. Lett.* **117,** 210502 (2016).
30. Prevedel, R. *et al.* High-speed linear optics quantum computing using active feed-forward. *Nature* **445,** 65–69 (2007).

Figures

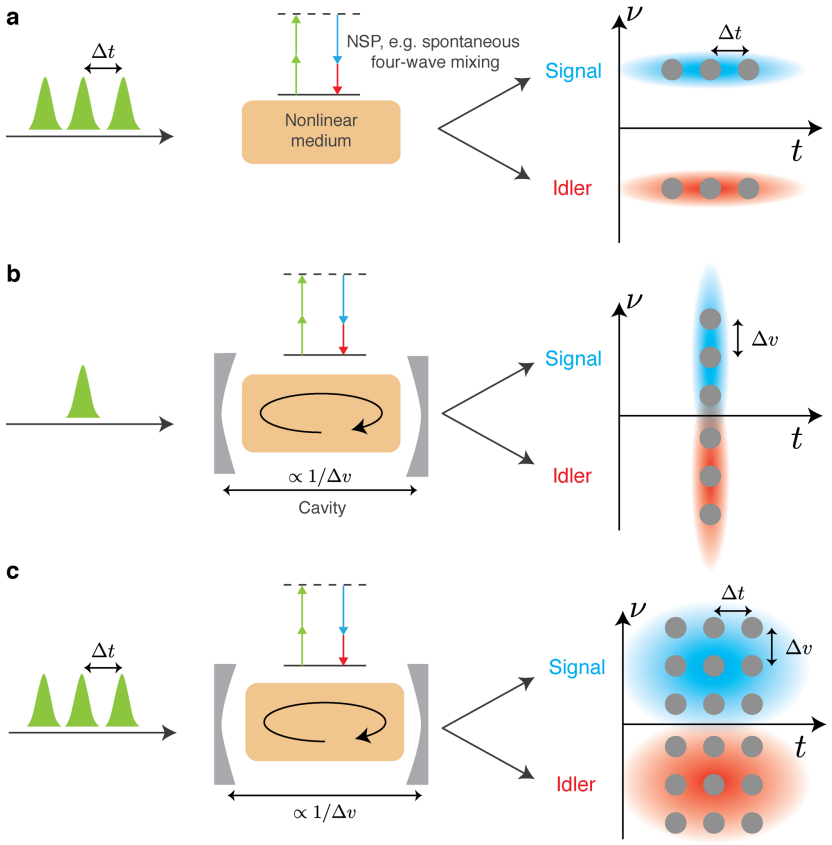

Fig. 1: Time-frequency hyper-entanglement scheme. a) An optical pulse train (composed of three pulses in this example) excites a nonlinear medium where photon pairs (signal and idler) are simultaneously generated via a Nonlinear Spontaneous Process (NSP, here four-wave mixing), in a superposition of several time modes (here d = 3, given by the number of pulses) generating a d-level time-bin entangled two-photon state. **b)** A single pulse excites a nonlinear medium placed inside a cavity (composed by two semi-reflective mirrors), where photon pairs are created over a broad bandwidth in a superposition of several spectral modes (here d = 3, given by the number of selected cavity resonances per photon), leading to a d-level frequency-bin entangled state. **c)** An optical pulse train excites a nonlinear cavity (merging the concepts of **a** and **b)** generating a simultaneously time- and frequency-bin entangled photon pair, i.e. a d-level hyper-entangled state.

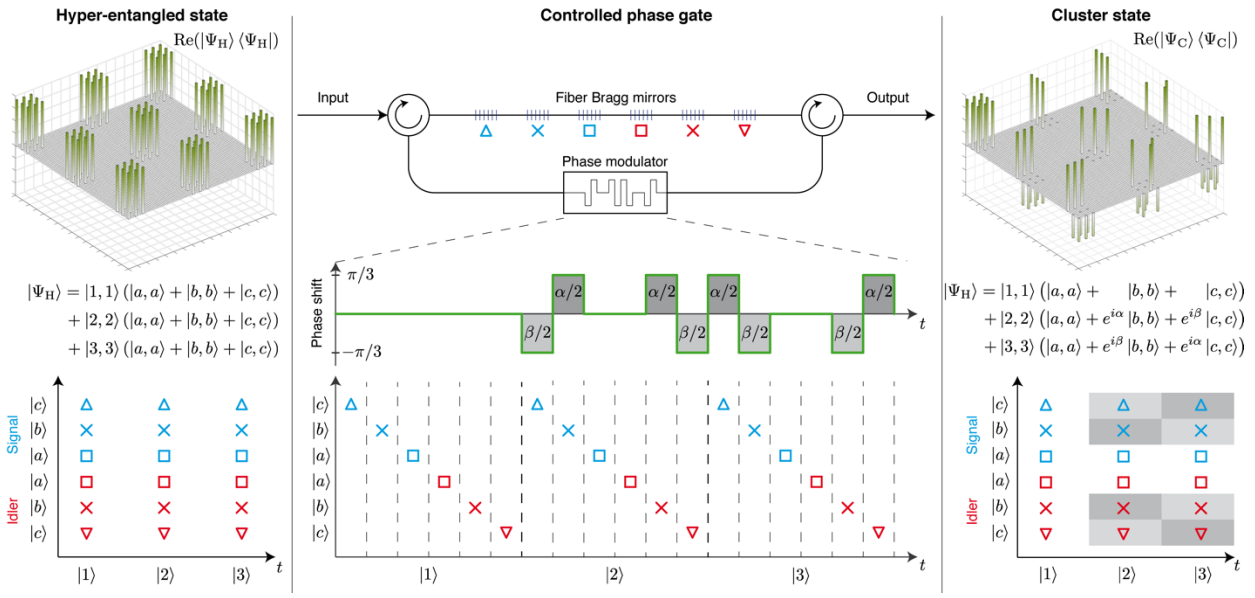

Fig. 2: Generation of d-level cluster states with a controlled phase gate. The two-photon d-level hyper-entangled state is simultaneously composed of three temporal modes $|1\rangle, |2\rangle,$ and $|3\rangle$ and three frequency modes $|a\rangle, |b\rangle$ and $|c\rangle$ per signal and idler photon, given by the state wave function $|\Psi_H\rangle$ (the real part of the associated density matrix is depicted in the top left panel). A controlled phase gate gives access to the individual terms of the quantum state. This was realized by temporally dispersing the individual frequency modes into different time slots via a fiber Bragg grating array (i.e. by means of frequency-to-time mapping) such that each individual state term has its own time slot (see middle panel). An electro-optical modulator was used to change the phase of the individual state terms, here by $\alpha/2$ and $\beta/2$ (see middle panel). The photons then enter the fiber Bragg grating array from the opposite end, such that the frequency-to-time mapping is coherently reversed. By choosing the phases $\alpha = 2\pi/3$ and $\beta = -2\pi/3$ the hyper-entangled state is transformed into a d-level cluster state $|\Psi_C\rangle$, where the two gray shading tones indicate the two opposite phase changes (the real part of the associated density matrix is shown in the top right panel).

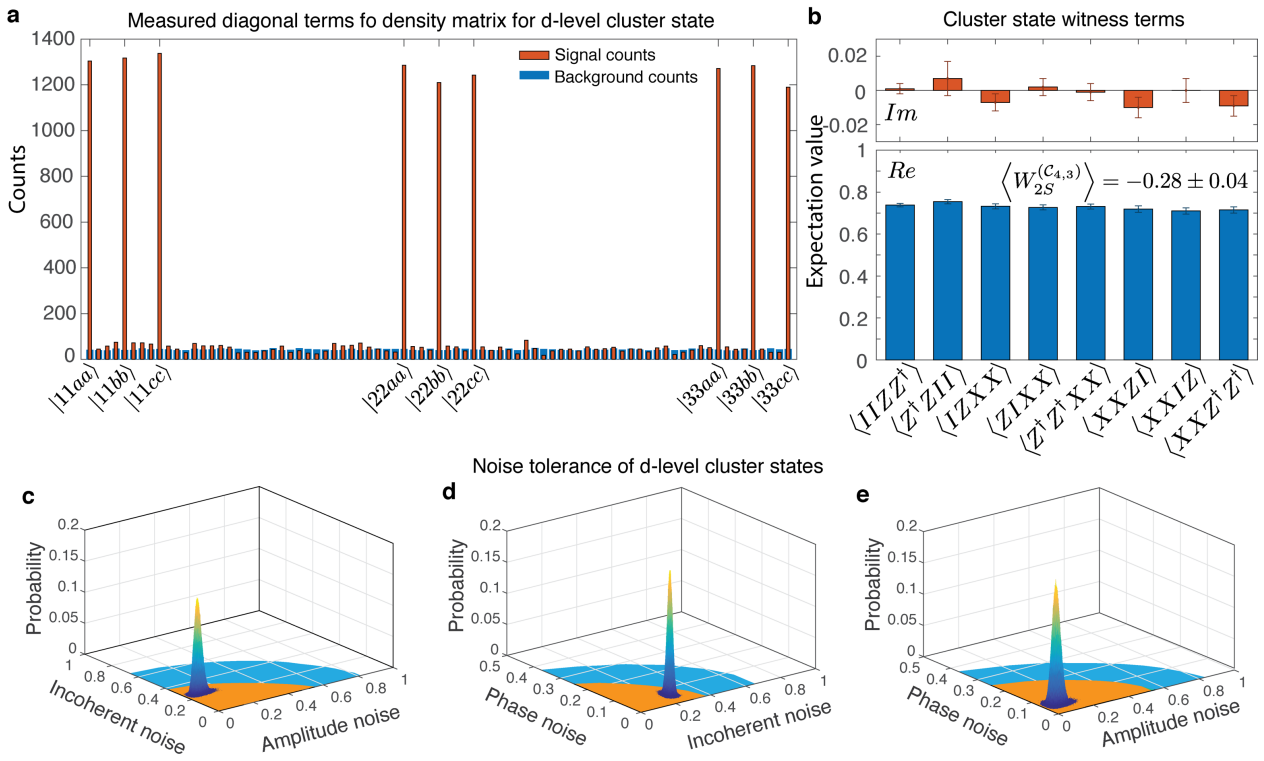

Fig. 3: Experimental demonstration of cluster state generation and related noise characteristics. a) Measured photon projections on the 81 diagonal elements of the state density matrix (Fig. 2, top right); each individual measurement had a duration of 1200 seconds. **b)** Real (blue bars) and imaginary (red bars) parts of the measured expectation values for the individual terms of the cluster state witness operator. Note that the expectation value for each term can be complex due to the non-Hermitian properties (imaginary eigenvalues) of the generalized Pauli matrices; however, only the eight real parts contribute to the witness expectation value, measured to be - 0.28 ± 0.04, which is always real, see Methods. **c-e)** Monte Carlo simulations for different noise contributions. The regions for which the optimal and measured witness operators confirm the existence of a cluster state for different sources of noise are indicated by blue- and orange-shaded areas, respectively. The witness bounds are shown for combinations of **c)** incoherent and amplitude noise, **d)** phase and incoherent noise, as well as **e)** amplitude and phase noise. The measurements (peaks in the respective diagrams) indicate that the largest contributor to state imperfection in our system is incoherent noise.

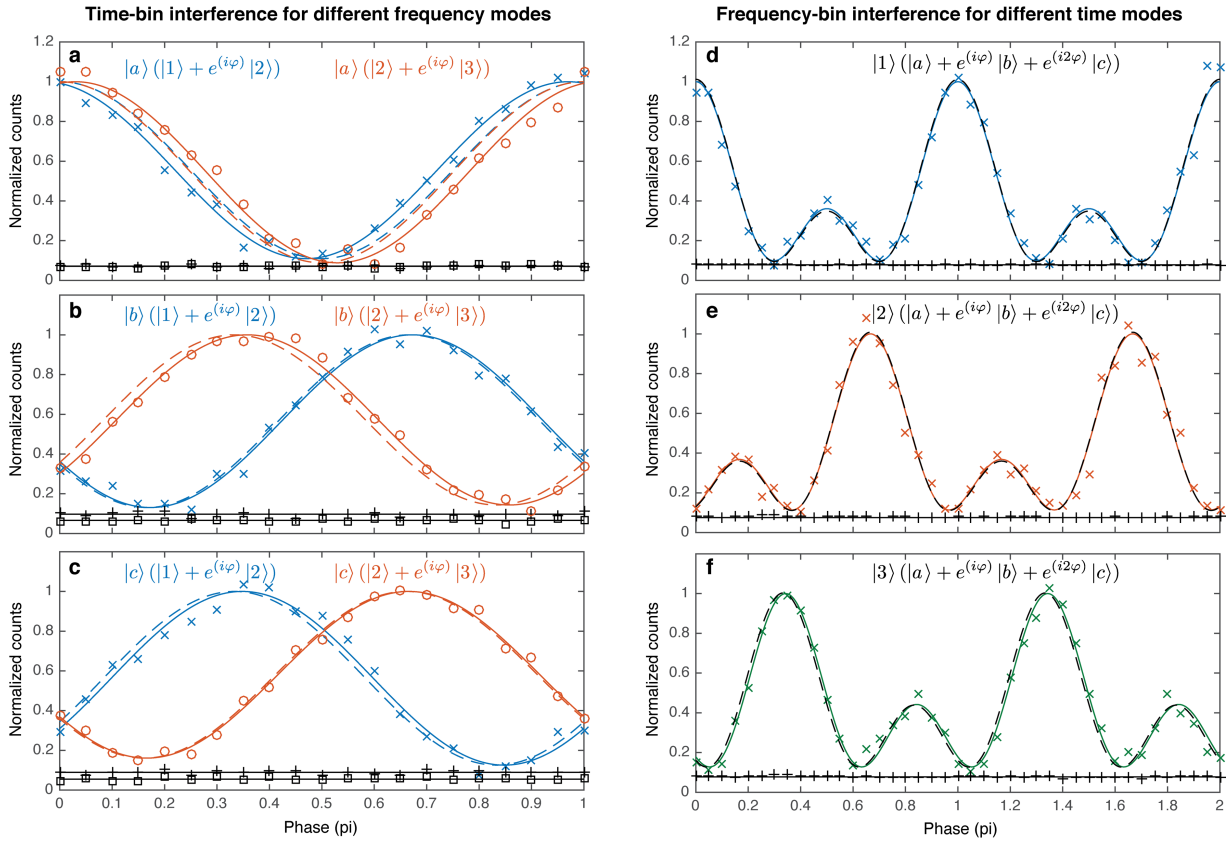

Fig. 4: High-dimensional one-way computation operations by measurement-based generation of orthogonal d-level two-party entangled quantum states. The cluster state was projected on specific time- and frequency-modes, resulting in different, orthogonal two-partite three-level entangled states in the frequency- and the time-domain, respectively. Quantum interference measurements were performed to confirm the presence of these two-partite states, as well as their entanglement. The time-bin quantum interference (**a, b, c**), measured by selecting two temporal modes, results in different phase-shifts (the relative position of the maximum with respect to the zero phase) after projecting the cluster states on the frequency modes $\{|aa\rangle, |bb\rangle, |cc\rangle\}$. Likewise, the frequency-bin quantum interference (**d, e, f**) measured by selecting three frequency modes, results in different phase-shifts after projecting the cluster state on the temporal modes $\{|11\rangle, |22\rangle, |33\rangle\}$. The quantum interferences follow the expected functions for the ideal, orthogonal two-partite states (dashed line: theory, solid line: fit); furthermore, the visibilities violate the respective Bell inequalities, see Methods. The measured phase values, together with the visibility, confirm the generation of orthogonal entangled qudit states through measurement-based operation, thus demonstrating high-dimensional one-way quantum computation operations.

Methods:

Experimental setup. The full experimental setup including all components is shown in Extended Data Figure 1. To generate phase-locked triple pulses, we used a carrier-envelope phase (CEP) stabilized mode-locked laser (Menlo Systems Inc.) operating at 250 MHz repetition rate (i.e. 4 ns pulse separation) and locked the CEP frequency to 250/6 = 41.667 MHz. We then employed an electro-optic intensity modulator, driven by an arbitrary waveform generator (Tektronix), to temporally gate triple pulses that were separated by 24 ns (i.e. taking each 6th pulse from the initial pulse train), where the set of pulses was repeated at a rate of 10 MHz (i.e. every 100 ns). The triple pulses were then spectrally filtered, amplified and coupled into the microring resonator at the resonance wavelength of 1555.93 nm. The microring resonator was fabricated from a high refractive index glass[10], with a free spectral range of 200 GHz and a Q-factor of 235,000 [31,32]. The input and output waveguides were featured by mode converters and were connected to polarization-maintaining fibers, resulting in coupling losses of <1.6 dB per facet. The average pump power coupled through the chip was 2.4 mW, measured at the drop-port. After the microring resonator, the excitation field was removed using a high-isolation (150 dB) notch filter, and the entangled photons were coupled into the controlled phase gate (see Fig. 2). This allowed to generate a hyper-entangled state[23,33] simultaneously exploiting the time-bin[34] and frequency-bin[35] approach. The phase-gate achieved frequency-to-time mapping via a custom-made fiber Bragg grating (FBG) array, consisting of six independent FBGs matched to the photon wavelengths (1551.08, 1552.70, 1554.31, 1557.55, 1559.17 and 1560.80 nm) and spatially separated in the fiber to achieve a 3.96 ns temporal delay between adjacent frequency modes (i.e. to introduce the frequency-time mapping). The FBGs were written into a photosensitive and deuterium loaded polarization-maintaining fiber (Nufern) using a 213 nm wavelength laser (5th harmonic of a Nd:YBO laser, Xiton Photonics Inc.) by means of a continuous writing scheme, realized in a tunable Talbot

interferometer with a moving fiber[36]. The FBGs were apodized using a squared cosine function, implemented by means of moving the Talbot phase mask with a piezo actuator[36]. The FBGs were then heated to 80°C for 48 hours to remove the deuterium, thus decreasing losses. They were subsequently spliced to standard polarization-maintaining Panda fibers using a tapered splice to decrease mode-matching losses. To implement the optical phase modulation within the gate, we used an electro-optic phase modulator (EOSpace), which was driven by an arbitrary waveform generator (Tektronix), synchronized to the 10 MHz reference clock of the mode-locked laser. After the phase-gate, the photons were sent to a computer-controlled amplitude and phase filter with two output ports (Finisar Waveshaper). This filter was used to route the photons to different characterization setups. One output was connected to a stabilized fiber interferometer with 24 ns unbalance to perform temporal projection measurements[9,37], and the other output was connected to an electro-optic phase modulator, which mixes different frequency components to perform frequency projection measurements[10,38,39]. Finally, the photons were separated using spectral programmable filters and sent to superconducting single photon detectors (Quantum Opus).

Entanglement witness for cluster states of qutrits. Multi-partite entangled quantum systems provide powerful resources for the implementation and advancement of many such applications[40]. The presence of a genuine pure multi-partite quantum state $|\psi\rangle$, and those states close to them (e.g. states degraded by noise) can be identified by measuring the expectation value of an entanglement witness operator[41]:

$$\widehat{\mathcal{W}} = \delta \cdot \mathbb{I} - |\psi\rangle\langle\psi|$$

with $\mathbb{I}$ being identity. The factor δ has to be chosen in such a way to exclude all bi-separable quantum states[41]. This witness detects the presence of the target state if the expectation value of

the witness is negative. For convention, we normalize this witness such that the optimal state results in an expectation value of minus one:

$$\mathcal{W} = \frac{1}{1-\delta}(\delta \cdot \mathbb{I} - |\psi\rangle\langle\psi|)$$

The factor δ is given by the square of the largest Schmidt coefficient of *all* singlet states between *any* combination of qutrits[41,42]. Determining this for cluster states is straight forward, since a cluster state can be projected under local operations on maximally entangled singlet states between any combination of qutrits. This immediately leads to the fact that the maximal Schmidt coefficient of a three-level cluster state when performing Schmidt-mode decomposition with respect to an arbitrary bipartite split does not exceed the maximal Schmidt coefficient of the singlet[43], which is given by $1/\sqrt{3}$ for three-level cluster states. This means that $\delta = \frac{1}{3}$ for a four qutrit cluster state. The optimal witness operator for a four partite, three-level cluster state $|C_{4,3}\rangle$ is therefore given by:

$$\mathcal{W}_{opt}^{(C_{4,3})} = \frac{1}{2}\mathbb{I} - \frac{3}{2}|C_{4,3}\rangle\langle C_{4,3}|$$

Measuring the optimal witness would require full state tomography, which is experimentally very demanding. For this reason, the optimal witness is usually reduced to a witness that only includes two orthogonal measurement settings[42], which can be achieved for cluster states using the stabilizer formalism[42]. Stabilizers are operators that are expressed as products of (generalized) Pauli matrices and are thus locally measurable by means of single-quDit projection measurements. Following the stabilizer formalism for d-level cluster states, developed in Ref. [7], we determined the stabilizers of the generated three-level, four-partite cluster state. In general, cluster state $|C_{N,d}\rangle$ can be uniquely defined by a set of main eigenvalue equations, where N is the number of parties and d the number of levels. These equations are:

$$X_a \bigotimes_{b \in \mathcal{N}(a)} Z_b \, |\mathcal{C}_{N,d}\rangle = |\mathcal{C}_{N,d}\rangle,$$

where a denotes the quDit and

$$\mathcal{N}(a) = \begin{cases} \{2\}, & a = 1 \\ \{N-1\}, & a = N \\ \{a-1, a+1\}, & a \notin \{1, N\} \end{cases}$$

denotes the neighbors of the quDit a. In the case of four qutrits, there is a set of four main eigenvalue equations that uniquely describe the cluster state $|C_{4,2}\rangle$ generated here, i.e.

$$S_i^{(C_{4,3})}|C_{4,3}\rangle = |C_{4,3}\rangle$$

with

$$S_1^{(C_{4,3})} = Z_1^\dagger Z_2 \mathbb{I}_3 \mathbb{I}_4,$$

$$S_2^{(C_{4,3})} = X_1 X_2 Z_3 \mathbb{I}_4,$$

$$S_3^{(C_{4,3})} = \mathbb{I}_1 Z_2 X_3 X_4,$$

$$S_4^{(C_{4,3})} = \mathbb{I}_1 \mathbb{I}_2 Z_3 Z_4^\dagger,$$

where X and Z are the generalized Pauli matrices, $\mathbb{I}$ is the Identity, and † denotes the transpose conjugate. In particular

$$Z = \begin{pmatrix} 1 & 0 & 0 \\ 0 & q & 0 \\ 0 & 0 & q^2 \end{pmatrix}, X = \begin{pmatrix} 0 & 0 & 1 \\ 1 & 0 & 0 \\ 0 & 1 & 0 \end{pmatrix}, \mathbb{I} = \begin{pmatrix} 1 & 0 & 0 \\ 0 & 1 & 0 \\ 0 & 0 & 1 \end{pmatrix},$$

with $q = e^{i2\pi/3}$. The matrices composing the stabilizers belong to the orthonormal Pauli group [44] $P = \{I, X, X^\dagger, Z, Z^\dagger, Y, Y^\dagger, V, V^\dagger\}$, with $Y = XZ,\ V = XZ^\dagger$.

Using the stabilizers, the density matrix of the cluster state can be written as

$$|C_{4,3}\rangle\langle C_{4,3}| = \prod_{k=1}^{4} \frac{S_k^{(C_{4,3})} + S_k^{\dagger(C_{4,3})} + \mathbb{I}}{3}$$

We can separate the stabilizers into two orthogonal sets that only include X and Z [42], which leads to a witness operator that only contains two measurement settings:

$$\mathcal{W}_{2S}^{(\mathcal{C}_{4,3})} = 2\mathbb{I} - \frac{3}{2}\prod_{even}^{4}\frac{S_k^{(C_{4,3})} + S_k^{\dagger(C_{4,3})} + \mathbb{I}}{3} - \frac{3}{2}\prod_{odd}^{4}\frac{S_k^{(C_{4,3})} + S_k^{\dagger(C_{4,3})} + \mathbb{I}}{3}$$

Considering the stabilizers listed above, this witness has an expectation value of:

$$\langle \mathcal{W}_{2S}^{(\mathcal{C}_{4,3})} \rangle = \frac{5}{3} - \frac{1}{3}Re\big(\langle \mathbb{I}_1\mathbb{I}_2Z_3Z_4^\dagger\rangle + \langle Z_1^\dagger Z_2\mathbb{I}_3\mathbb{I}_4\rangle + \langle \mathbb{I}_1Z_2X_3X_4\rangle + \langle \mathrm{X}_1X_2Z_3\mathbb{I}_4\rangle + \langle Z_1\mathbb{I}_2X_3X_4\rangle$$
$$+ \langle Z_1^\dagger Z_2^\dagger X_3X_4\rangle + \langle X_1X_2\mathbb{I}_3Z_4\rangle + \langle X_1X_2Z_3^\dagger Z_4^\dagger\rangle\big),$$

where *Re( )* refers to the real-part of the operators, and considering that the real part of an imaginary number *C* is given by $Re(C) = \frac{C+C^\dagger}{2}$. The witness operator therefore always has a real expectation value, as required for a measurable value with physical meaning. Note that the generalized Pauli matrices (i.e. for d-level systems) are non-Hermitian and have complex eigenvalues, and therefore the expectation values of the individual stabilizers can have imaginary components.

In a similar way as described above, witnesses were previously derived for cluster states of qubits[42]. The optimal witness for all cluster states of qubits is given by

$$\mathcal{W}_{opt}^{(\mathcal{C}_{N,2})} = \mathbb{I} - 2\big|C_{N,2}\big\rangle\big\langle C_{N,2}\big|$$

Which results in a noise tolerance for a cluster state of qubits mixed with linear incoherent noise of 50%. The reduced witness for cluster states of qubits was derived in Ref. [42], and reads:

$$\mathcal{W}_{2S}^{(\mathcal{C}_{N,2})} = 3\mathbb{I} - 2\prod_{even}^{N}\frac{S_k^{(C_{N,2})} + \mathbb{I}}{2} - 2\prod_{odd}^{N}\frac{S_k^{(C_{N,2})} + \mathbb{I}}{2}$$

This witness for qubits has a noise tolerance with respect to incoherent linear noise of 33.33% for four qubits, and 28.57% for six qubits[42].

Measurement of witness expectation value. To measure the expectation value of the entanglement witness, the individual expectation values eight stabilizers have to be measured separately. Each stabilizer expectation value can be extracted by means of 81 separate measurements, which can be performed by projecting the state on the respective combinations of the stabilizer eigenvectors. In particular, the witness terms $Z_1^\dagger Z_2 I_3 I_4$ and $I_1 I_2 Z_3 Z_4^\dagger$ have eigenvectors $|1\rangle$, $|2\rangle$, $|3\rangle$, $|a\rangle$, $|b\rangle$, and $|c\rangle$; while $I_1 Z_2 X_3 X_4$, $Z_1 I_2 X_3 X_4$ and $Z_1^\dagger Z_2^\dagger X_3 X_4$ have eigenvectors $|1\rangle$, $|2\rangle$, $|3\rangle$, $|f1\rangle$, $|f2\rangle$, and $|f3\rangle$, with $|f1\rangle = |a\rangle + |b\rangle + |c\rangle$, $|f2\rangle = |a\rangle + e^{i2\pi/3}|b\rangle + e^{-i2\pi/3}|c\rangle$, $|f3\rangle = |a\rangle + e^{-i2\pi/3}|b\rangle + e^{i2\pi/3}|c\rangle$; finally $X_1 X_2 Z_3 I_4$, $X_1 X_2 I_3 Z_4$ and $X_1 X_2 Z_3^\dagger Z_4^\dagger$ have eigenvectors $|t1\rangle$, $|t2\rangle$, $|t3\rangle$, $|a\rangle$, $|b\rangle$, and $|c\rangle$, with $|t1\rangle = |1\rangle + |2\rangle + |3\rangle$, $|t2\rangle = |1\rangle + e^{i2\pi/3}|2\rangle + e^{-i2\pi/3}|3\rangle$, $|t3\rangle = |1\rangle + e^{-i2\pi/3}|2\rangle + e^{i2\pi/3}|3\rangle$. To extract all projection values, 3∗81=242 parameters, which can take real values between zero and one, have to be experimentally determined. From these 242 measurement outcomes, the expectation values of the individual witness terms (stabilizers) can be calculated, which are complex numbers with an absolute smaller than one. The witness is then calculated from the real parts of the eight stabilizer terms. Projections on time and frequency modes ($|1\rangle$, $|a\rangle$, etc.), as well as frequency-bin superpositions ($|f1\rangle$, etc.) can be immediately obtained with the experimental setup. Projections on time-bin superpositions were achieved as follows: We assessed the state phases through simultaneous projection measurements on the superposition of two time-bins each, implemented by unbalanced two-arm interferometers. The time-bin projections $|t1\rangle$, $|t2\rangle$ and $|t3\rangle$ were then reconstructed taking into account the measured interference patterns.

Extraction of amplitude and phase terms of the wave function. The most generic wave function to express the four qutrit hyper-entangled states is

$$|\Psi\rangle = m_{1,a}|1,1,\mathrm{a},\mathrm{a}\rangle + m_{1,b}|1,1,\mathrm{b},\mathrm{b}\rangle + m_{1,c}|1,1,\mathrm{c},\mathrm{c}\rangle$$

$$+m_{2,a}|2,2,\mathrm{a},\mathrm{a}\rangle + m_{2,b}|2,2,\mathrm{b},\mathrm{b}\rangle + m_{2,c}|2,2,\mathrm{c},\mathrm{c}\rangle$$

$$+m_{3,a}|3,3,\mathrm{a},\mathrm{a}\rangle + m_{3,b}|3,3,\mathrm{b},\mathrm{b}\rangle + m_{3,c}|3,3,\mathrm{c},\mathrm{c}\rangle,$$

where $m_{t,f} = |m_{t,f}|e^{i\phi_{t,f}}$ are complex numbers with amplitude $|m_{t,f}|$ and phase $\phi_{t,f}$. Here, $t = 1, 2, 3$ and $f = a, b, c$. We determined the amplitudes by performing 81 coincidence measurements between all combinations of temporal and frequency modes, and confirmed that, as expected, the wave function only has the above-stated nine non-zero elements, see Figure 3a). To extract the phases $\phi_{t,f}$, we used the nine quantum interference measurements shown in Fig. 4. We then fitted the predicted functions to the quantum interference patterns in order to extract the individual phases of the wave function, listed in Table S1, including the estimated error for these values. All measured visibilities exceed the threshold (also shown in Table S1) required to violate two-partite Bell inequalities[45].

Witness distribution and noise characterization via Monte Carlo simulations. We performed Monte Carlo simulations to infer the distribution of the witness expectation value. Starting from the measured input values and their determined experimental errors, we assumed a Gaussian error distribution for each individual input parameter and calculated the witness expectation value one million times. These calculations were then summarized in normalized histograms, see Fig. 3. To determine the witness bound for different sources of input noise (i.e. incoherent, amplitude, and phase noise), we calculated the associated operator for input parameters with different noise sources and average strengths. In each calculation, only two noise sources were considered at a time, while the remaining noise source was kept at zero. For diagrams involving incoherent noise, a fixed value for incoherent noise was first set and ten million random input values for either the phases or amplitudes were generated (then the incoherent noise value was changed for different rounds of simulations). For the diagrams where both amplitude and phase noise were open

parameters, we generated one billion random input settings. For each simulation input, we calculated the witness expectation value. The outcomes were then sorted according to positive and negative witness values as well as their average noise. We defined the amplitude noise as the average over the absolute deviations from the ideal value, normalized by the latter: $\sigma_{ampl.} = 3 * \frac{1}{9}\sum|a_i - 1/3|$, where a_i are the nine different amplitude values in the wave function and 1/3 is the ideal value. We define the phase noise as the average over the absolute phase deviation from the ideal value, normalized by the optimal phase terms: $\sigma_{ampl.} = \frac{3}{2\pi} * \frac{1}{9}\sum|\theta_i - \varphi_{ideal}|$, where $\varphi_{ideal} = [0, \frac{2\pi}{3}, \frac{-2\pi}{3}]$ are the ideal phase settings, and θ_i are the nine different determined phase values in the wave function. The stated bound for the witness was determined as the points where over 95% of all calculated witness values were negative.

Author contribution: C.R. and M.K. contributed equally. M.K., C.R., P.R., and S.S. developed the idea. C.R., M.K. P.R., M.I., Y.Z., L.R.C., and B.F. performed the measurements and analyzed the data. S.S., C.R., M.K., L.C., and W.M. performed the theoretical analysis. S.T.C. and B.E.L designed and fabricated the microring resonator. S.L and R.K designed and fabricated the fiber Bragg gratings. D.J.M. and A.C. contributed to discussions. R.M and J.A. managed the project. All authors contributed to the writing of the manuscript.

Author information: Correspondence and requests for materials should be addressed to M.K. (michael.kues@glasgow.ac.uk) or R.M. (morandotti@emt.inrs.ca).

Data availability: The data that supports the plots within this paper and other findings of this study are available from the corresponding author upon reasonable request.

Methods References:

31. Moss, D. J., Morandotti, R., Gaeta, A. L. & Lipson, M. New CMOS-compatible platforms based on silicon nitride and Hydex for nonlinear optics. *Nat. Photonics* **7,** 597–607 (2013).
32. Pasquazi, A. *et al.* Micro-combs: A novel generation of optical sources. *Phys. Rep.* **729,** 1–81 (2017).
33. Kwiat, P. G. Hyper-entangled states. *J. Mod. Opt.* **44,** 2173–2184 (1997).
34. Brendel, J., Gisin, N., Tittel, W. & Zbinden, H. Pulsed energy-time entangled twin-photon source for quantum communication. *Phys. Rev. Lett.* **82,** 2594–2597 (1999).
35. Olislager, L. *et al.* Frequency-bin entangled photons. *Phys. Rev. A* **82,** 013804 (2010).
36. Loranger, S., Karpov, V., Schinn, G. W. & Kashyap, R. Single-frequency low-threshold linearly polarized DFB Raman fiber lasers. *Opt. Lett.* **42,** 3864 (2017).
37. Xiong, C. *et al.* Compact and reconfigurable silicon nitride time-bin entanglement circuit. *Optica* **2,** 724 (2015).
38. Lukens, J. M. & Lougovski, P. Frequency-encoded photonic qubits for scalable quantum information processing. **4,** 8–16 (2017).
39. Imany, P. *et al.* 50-GHz-spaced comb of high-dimensional frequency-bin entangled photons from an on-chip silicon nitride microresonator. *Opt. Lett.* **26,** 1825–1840 (2018).
40. Hein, M., Eisert, J. & Briegel, H. J. Multiparty entanglement in graph states. *Phys. Rev. A* **69,** 062311 (2004).
41. Bourennane, M. *et al.* Experimental detection of multipartite entanglement using witness operators. *Phys. Rev. Lett.* **92,** 087902 (2004).
42. Toth, G. & Guehne, O. Entanglement detection in the stabilizer formalism. *Phys. Rev. A* **72,** 022340 (2005).
43. Nielsen, M. A. Conditions for a class of entanglement transformations. *Phys. Rev. Lett.* **83,** 436–439 (1999).
44. Lawrence, J. Mutually unbiased bases and trinary operator sets for N qutrits. *Phys. Rev. A* **70,** 012302 (2004).
45. Collins, D., Gisin, N., Linden, N., Massar, S. & Popescu, S. Bell inequalities for arbitrarily high-dimensional systems. *Phys. Rev. Lett.* **88,** 040404 (2002).

Extended Data

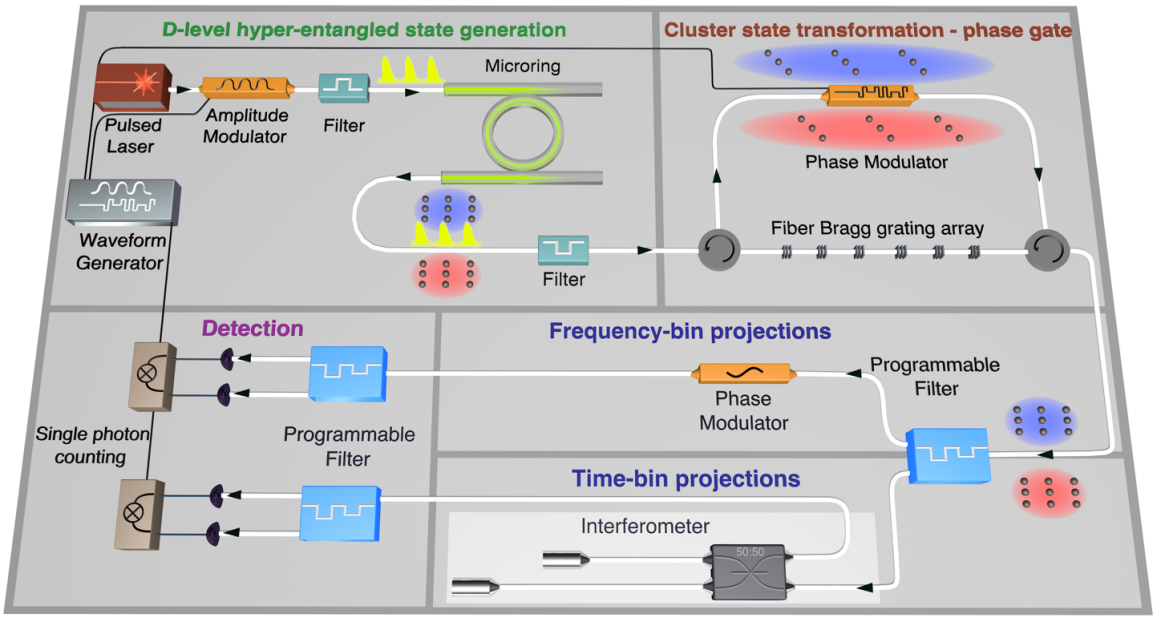

Extended Data Figure 1 | Experimental setup for generation of d-level cluster-states and performing measurement-based quantum computation operations. A mode-locked laser generated an optical pulse train from which three pulses were gated with an amplitude modulator driven by an arbitrary waveform generator. The triple pulses were sent though a filter into a highly nonlinear microring resonator on its resonance frequency. Within the ring resonator, two photons from the excitation field were converted into signal and idler photons (marked in red and blue) via spontaneous four-wave mixing. Those are generated in a superposition of three time and three frequency modes (indicated by bullets), forming a hyper-entangled state. A filter was used to reject the excitation field. The novel phase gate architecture provided individual access to amplitude and phase of the generated hyper-entangled state components. The phase gate consisted of a fiber Bragg grating array which allowed to map the different frequencies of the signal and idler photons into the time domain. A phase modulator, synchronized with the arbitrary waveform generator, was used to change the phase of the different state terms to produce d-level cluster states. After the frequency-to-time mapping was reversed, a programmable filter allowed to send the cluster state into two different analysis setups: 1) frequency-bin projections via frequency mixing though an electro-optic phase modulator, and 2) time-bin projections via an imbalanced interferometer. The photons were then separated by filters and measured with single-photon detectors.

Extended Data Table 1 | Phases and visibilities extracted from the quantum interference characterization for measurement-based generated frequency- and time-bin quDits from the cluster state

Projection	$\phi_{1,f} - \phi_{2,f}$	$\phi_{2,f} - \phi_{3,f}$	**Visibility $V^t_{(11,22)}$**	**Visibility $V^t_{(22,33)}$**
$\|aa\rangle$	-0.06 ± 0.02	0.06 ± 0.02	80.2 % > 70.7%	83.7 % > 70.7 %
$\|bb\rangle$	0.65 ± 0.02	-0.72 ± 0.03	76.7 % > 70.7 %	74.9 % > 70.7 %
$\|cc\rangle$	0.67 ± 0.02	-0.69 ± 0.03	77.6 % > 70.7 %	72.2 % > 70.7 %
	$\phi_{t,1} - \phi_{t,2}$	$\phi_{t,1} - \phi_{t,3}$	**Visibility $V^f_{(aa,bb,cc)}$**	
$\|11\rangle$	0.087 ± 0.03	0.001 ± 0.03	0.83 % > 77.4%	
$\|22\rangle$	-0.594 ± 0.03	0.667 ± 0.03	0.80 % > 77.4%	
$\|33\rangle$	0.638 ± 0.02	-0.628 ± 0.02	0.79 % > 77.4%	